EES Solar

PAPER

View Article Online
View Journal | View Issue



Cite this: *EES Sol.*, 2026, **2**, 127

# Cooperative phase–interface modulation enabling ultralow voltage loss in bromide-containing perovskite solar cells with isopropanol as an antisolvent

Bo Zhou,†[ab] Minh Anh Truong,†[c] Junxue Guo,[ad] Qian Li,[be] Wei Yu,[ab] Xin Guo,[ab] Atsushi Wakamiya *[c] and Jiewei Liu *[a]

Isopropanol (IPA), as a green and low-cost antisolvent, can induce humidity-stable (111)-oriented perovskite films. However, its rapid extraction rate often leads to wrinkle formation and surface damage, while resulting in unwanted residual $PbI_2$. Consequently, it has been challenging to adopt IPA in inverted (p-i-n) devices, particularly for bromide-containing perovskite solar cells (PSCs). To address these issues, we developed a cooperative phase–interface modulation strategy that simultaneously optimizes both bulk and surface of Br-containing perovskite. For the first time, we reveal an IPA-driven topological correlation between the (111) orientation and $\delta$-$FAPbI_3$. Leveraging this insight, the use of same umbrella-like structured IPA and isopropylammonium chloride (iPAmCl) binary additives mitigates rapid crystallization while retaining the preferred (111) orientation. Meanwhile, surface treatment with trifluoromethyl-benzylamine hydroiodide ($CF_3$PMAI) reconstructs the damaged surface and passivates sub-surface defects. The strong dipole effect also converts the surface from p- to n-type, forming a spontaneous p-n facet homojunction with the (111) facet bulk. Benefiting from improved energy level alignment and suppressed nonradiative recombination, the quasi-Fermi level splitting (QFLS) was effectively enhanced. As a result, a record $V_{OC}$ of 1.24 V was achieved for a 1.62 eV perovskite device, with a highest PCE of 24.33% and excellent storage stability, marking the first successful application of an environmentally friendly antisolvent in Br-containing PSCs with an ultralow voltage loss of 0.38 V. This study establishes a mechanistic framework for minimizing voltage loss of high-performance PSCs.

Received 15th November 2025
Accepted 19th November 2025

DOI: 10.1039/d5el00189g

rsc.li/EESSolar



## Broader context

Perovskite solar cells face critical sustainability-performance trade-offs: toxic antisolvents (*e.g.*, chlorobenzene) enable high efficiency but pose health risks, while bromide-containing compositions suffer from severe voltage losses (>0.45 V) due to phase segregation. Although green isopropanol (IPA) offers eco-friendly processing, its rapid crystallization degrades Br-perovskite quality. This work pioneers a cooperative phase–interface modulation strategy harmonizing solvent engineering and defect control. Using IPA to drive (111)-oriented crystallization, we introduce binary additives (IPA/iPAmCl) to regulate kinetics and preserve subsurface integrity. Crucially, custom trifluoromethyl-benzylamine hydroiodide ($CF_3$PMAI) passivation eliminates deep traps and induces a p-to-n sub-surface transition, creating carrier-extracting homojunctions. The resulting 1.62 eV Br-containing PSCs achieve an ultralow voltage loss of 0.38 V (93% of the SQ limit) and 24.33% efficiency—among the highest reported for IPA-processed devices—along with >90% stability retention over 3000 hours. This study marks a successful integration of a green antisolvent into high-performance Br-containing PSCs, demonstrating that environmental sustainability and cutting-edge performance can coexist. Beyond photovoltaics, our cooperative phase–interface modulation strategy establishes a universal framework for defect management in halide-mixed semiconductors, accelerating the development of eco-processed optoelectronics for solar cells and beyond.

[a]*State Key Laboratory of Photoelectric Conversion and Utilization of Solar Energy, Dalian National Laboratory for Clean Energy, Dalian Institute of Chemical Physics, Chinese Academy of Sciences, Dalian 116023, China. E-mail: jwliu@dicp.ac.cn*

[b]*University of Chinese Academy of Sciences, Beijing 100049, China*

[c]*Institute for Chemical Research, Kyoto University, Gokasho Uji, Kyoto, 611-0011, Japan. E-mail: wakamiya@scl.kyoto-u.ac.jp*

[d]*School of Chemistry and Materials Science, University of Science and Technology of China, Hefei 230026, China*

[e]*State Key Laboratory of Catalysis, Dalian Institute of Chemical Physics, Chinese Academy of Sciences, Dalian 116023, China*

† These authors contributed equally to this work.

## Introduction

An efficient approach to obtain high-quality perovskite thin films with one-step deposition involves the use of antisolvents, which facilitate controlled crystallization and film uniformity. Commonly used antisolvents, such as chlorobenzene (CB) and toluene (TL), are low-polarity aromatic compounds that provide the supersaturation driving force necessary for the formation of perovskite films.[1] Unfortunately, these antisolvents are

cytotoxic, carcinogenic, and pose irreversible health hazards.[2] To address these concerns, isopropanol (IPA), a green and inexpensive alternative, has shown great potential due to its non-toxic nature (Fig. 1c). In recent years, the application of IPA as an antisolvent has been developed, enabling n-i-p structured perovskite solar cells (PSCs) with power conversion efficiencies (PCEs) of up to 23%.[3] However, its application in the p-i-n inverted structure remains relatively underexplored, presenting substantial research value and the potential to extend its broader applicability to bromide-containing perovskite systems. Moreover, IPA can trigger the perovskite to adopt a preferred (111) orientation, which exhibits improved carrier mobility, suppressed cationic migration, and enhanced device stability[4] (Fig. 1b, S2 and3). As shown in Fig. S1, the uniform stacking of the (111) orientation holds great potential for achieving low $V_{OC}$ losses. However, the relatively low boiling point (82.3 °C) and high volatility of IPA frequently result in poor film morphology and a high density of defects, particularly in bromide-containing perovskite systems, thereby limiting the achievable PCE. Although IPA-processed films can exhibit an improved $V_{OC}$

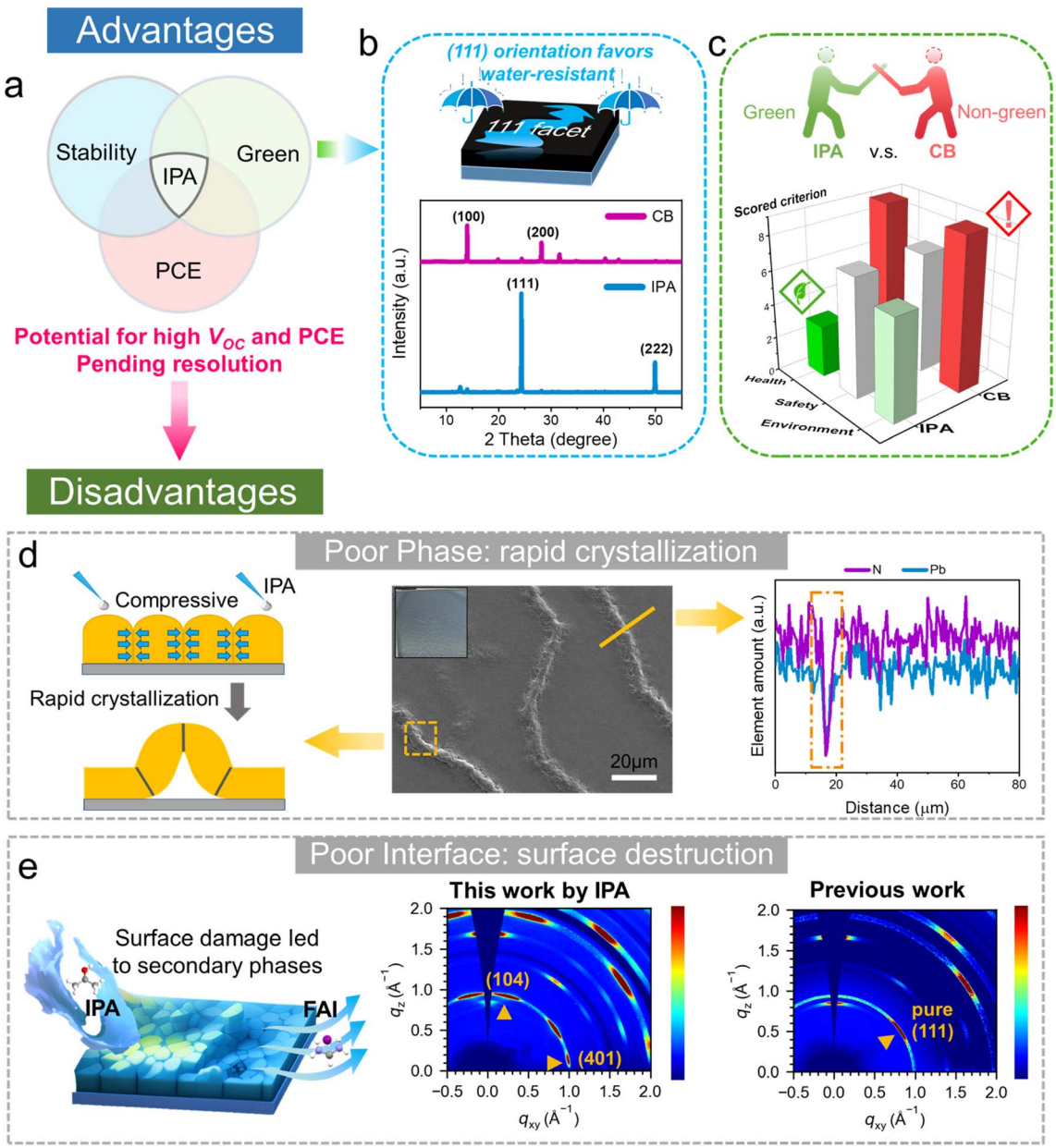


Fig. 1 The advantages and disadvantages of isopropanol (IPA) as an antisolvent. (a) Conceptual diagram highlighting the significance of this work. (b) Film orientation under different antisolvent treatments. (c) Scored criteria related to health, safety, and environment based on AstraZeneca's guidelines.[12] (d) Schematic illustration of rapid crystallization induced by IPA, accompanied by corresponding scanning electron microscopy (SEM) and energy-dispersive X-ray spectroscopy (EDS) results. (e) Schematic showing surface damage caused by IPA, along with corresponding Grazing-Incidence Wide-Angle X-ray Scattering (GIWAXS) data, clearly revealing secondary phases indexed to the (104) and (401) planes compared to our previous work.[6]

compared to those processed with CB, the $V_{OC}$ loss remains significant, indicating the need for further bulk or interfacial treatments (see discussion in Fig. S4S12).

Two main challenges with IPA need to be addressed, as shown in Fig. 1d and e: (1) considering the solubility of organic precursors in the antisolvent and their miscibility with the main solvent of the perovskite precursor solution, IPA is classified as a short-duration antisolvent.[5] The resulting rapid nucleation induced by IPA makes it challenging to precisely control the antisolvent application, leading to films with extremely rough surfaces and poor coverage, often exhibiting spiral patterns, cracks, and wrinkles (Fig. 1d). (2) Given that crystallization occurs from top to bottom in the wet film, IPA disrupts the surface region, leading to the formation of some $\delta$ phases and (104)/(401) secondary crystal facets, which were absent in previous work on (111)-oriented films[6] (Fig. 1e). Typically, IPA antisolvent leads to a $PbI_2$-rich surface,[7] making the surface more p-type. Meanwhile, the (111) orientation induced by IPA shows a tendency toward p-type behavior, which is advantageous for n-i-p structured devices but not suitable for pin inverted devices. These challenges are further compounded in bromide-containing perovskites, which are inherently more prone to phase separation and interface instability. To the best of our knowledge, no prior studies have demonstrated efficient Br-containing inverted devices processed with IPA as an antisolvent, making this both an unresolved and underexplored issue in the field.

To address these issues, we devised a cooperative phase–interface modulation strategy that simultaneously manages bulk and surface defects in perovskite films to achieve high-performance inverted PSCs. First, IPA and isopropylammonium chloride (iPAmCl)[8] binary additives—featuring similar branched-chain structures, here described as possessing an umbrella-like molecular configuration, were introduced into the precursor solution. These additives act as molecular anchors during the antisolvent process, stabilizing the transforms from (002)-oriented δ-$FAPbI_3$ to (111)-oriented α-$FAPbI_3$ and guiding crystallization, suppressing the formation of the undesirable $(100)_\delta$ phase and retaining the (111) orientation. Moreover, this strategy slows down the crystallization process, reducing film roughness and bulk defects.

While IPA offers a green alternative for perovskite film formation, its application in bromide-containing perovskite solar cells—promising candidates for tandem and semi-transparent applications—is particularly challenging, generally leading to significant $V_{OC}$ loss. Although bulk passivation strategies have proven effective in enhancing the PCE of Br-free perovskites, they fall short in addressing the issue of phase segregation commonly observed in Br-containing perovskites. To bridge this gap and further expand the understanding of Br-containing perovskite systems, trifluoromethyl-benzylamine hydroiodide ($CF_3PMAI$)[9] was introduced as a novel surface passivation agent, which promoted the digestion and ripening process as well as sub-surface reconstruction. In addition, it simultaneously passivated surface defects, converted it from p- to n-type, and stabilized the films against moisture with the help of the hydrophobic $-CF_3$ group. As a result, our custom-tailored devices achieve a remarkably enhanced efficiency of 24.33% with a record $V_{OC}$ of 1.24 V. To the best of our knowledge, the $V_{OC}$ loss of 0.38 V with respect to the 1.62 eV bandgap, as achieved here, is one of the lowest values reported for PSCs between 1.54 eV and 1.75 eV.[10,11] This work provides an effective and universal strategy for green antisolvents in Br-containing perovskites, pushing $V_{OC}$ closer to the Shockley–Queisser (S–Q) limit.

## Results and discussion

Notably, it is necessary to eliminate the negative effects of IPA as an antisolvent while retaining its advantage in inducing the (111) orientation. To do this, we must first understand the mechanism by how the antisolvent IPA induces this orientation. However, benefiting from the unique properties of IPA, the addition of IPA as an antisolvent quickly leads to a direct transformation from the precursor solution to black perovskite crystals, even without thermal annealing. To effectively monitor this rapid transformation, we used a low-temperature freezing method to preserve the state of the wet film immediately after IPA addition and then conducted a series of characterization studies (Fig. 2a). The procedure involves spin-coating the precursor with antisolvent treatment, followed by cryogenic quenching and immediate thermal annealing, during which *in situ* X-ray diffraction (XRD) or photoluminescence (PL) measurements are performed. The perovskite (PSK) films treated by CB and IPA are denoted as CB-PSK and IPA-PSK, respectively, hereinafter.

*In situ* XRD analysis revealed that when using conventional CB as an antisolvent, the high formation energy requirements of the black phase cannot be met, causing the dimethylsulfoxide (DMSO)-coordinated complex to rapidly and uncontrollably form both δ- and α-phase $FAPbI_3$ simultaneously (Fig. 2b and d). In this scenario, the perovskite tends to form the energetically favored (100) facet. In contrast, when IPA is used as the antisolvent, XRD indicates that the initial phase is primarily δ-$FAPbI_3$ dominated by the (002) facet, which then transitions to α-$FAPbI_3$ dominated by the (111) facet. The XRD peak positions and crystalline structures viewed from the *c*-axis of these two facets are remarkably similar, suggesting that IPA induces the (111) orientation during the δ- to α-$FAPbI_3$ phase transition (Fig. 2c). According to the solvent–solute compatibility principle, the spatial parameters of DMSO and IPA molecules are similar, and their branch-shaped configuration increases the probability of effective miscibility, facilitating IPA's rapid displacement of residual DMSO solvent. Additionally, given IPA's solubility for FAI, the hydrogen bond between IPA and FAI is strong, allowing a portion of IPA to remain and participate in the perovskite crystallization process.

We suggest a possible mechanism by how IPA alters the reaction pathway from the precursor to the desired (111)-$FAPbI_3$, as illustrated in Fig. 2e and S1323: IPA grafts onto the surface of the (002)-oriented $\delta$-$FAPbI_3$ by binding with $FA^+$, stabilizing this structure. As energy is absorbed during annealing, the surface layer acts as a template, then the edge-sharing octahedra of $\delta$-$FAPbI_3$ gradually changes to the

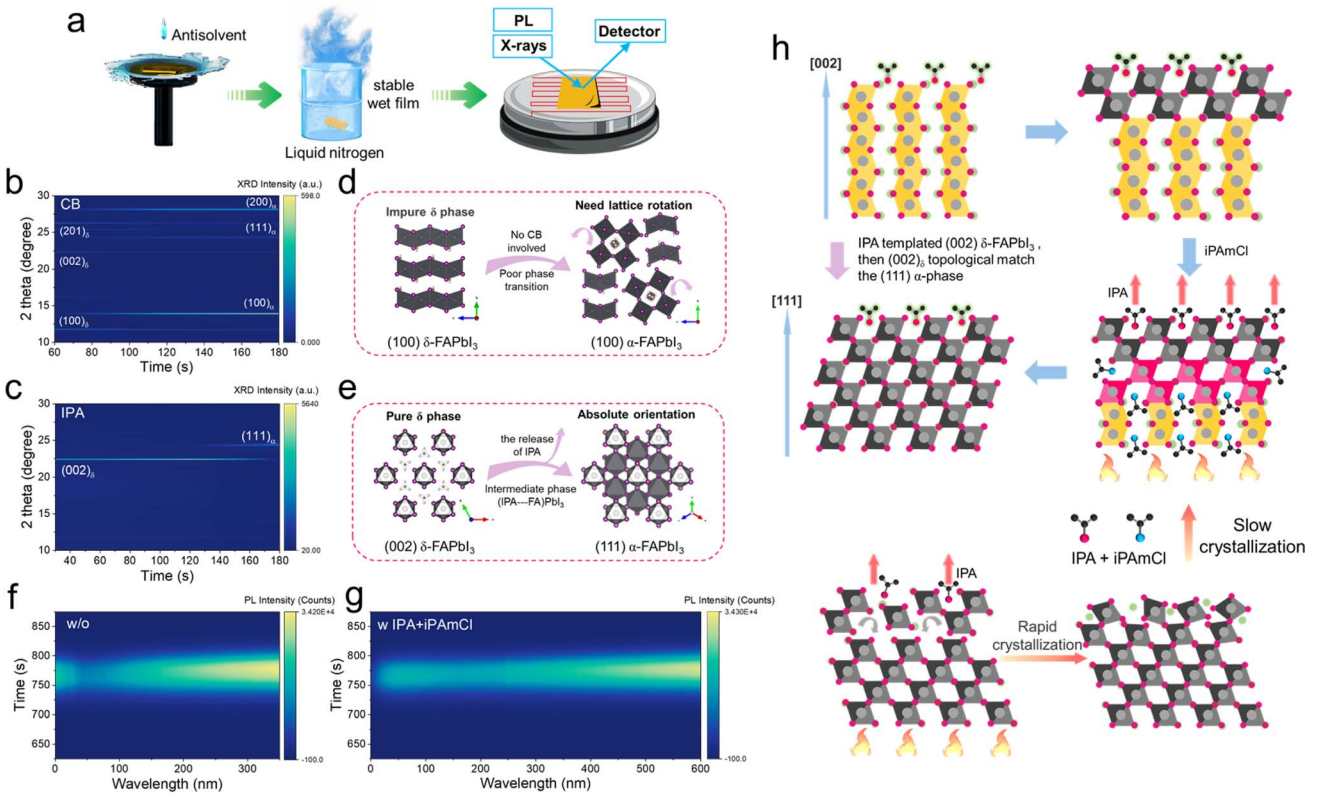


Fig. 2 Mechanistic discovery of IPA-induced crystallization. (a) Schematic illustration of *in situ* XRD and PL monitoring during the $FAPbI_3$ perovskite crystallization. (b and c) *In situ* XRD false-color intensity maps for the perovskite films fabricated by (b) CB and (c) IPA antisolvents, respectively. (d and e) Crystalline structures viewed showing δ-$FAPbI_3$ and α-$FAPbI_3$ phases and the phase transition between them. (f and g) Heat maps of *in situ* PL of the $FAPbI_3$ film under annealing for (f) control and (g) with BAs. (h) Schematic illustration for crystallization kinetics of IPA-induced orientation transition and crystallization routes to the α-$FAPbI_3$ film through thermal annealing for control or additive-assisted crystallization.

corner-sharing octahedra of α-$FAPbI_3$, resulting in a (111)-oriented perovskite. This controlled and complete phase transition from $(002)_\delta$ to $(111)_\alpha$, triggered by IPA, enables the formation of the (111) orientation. We can also identify corresponding intermediates formed with IPA during this transition. Based on this assumption, a series of antisolvents with molecular structures similar to IPA can be identified, allowing us to compare their diffraction intensity changes and explain the resulting orientation shifts (Fig. S21 and S22).

We selected a bulk additive with a similar umbrella-like configuration: the binary additives IPA and iPAmCl[13] were simultaneously incorporated into the precursor solution, while the film fabricated with IPA alone (without iPAmCl) is denoted as IPA(bulk)-PSK. Details regarding the choice and application method of the additives can be found in the SI. This section also demonstrates that adding these additives in the bulk does not affect the (111) orientation, as the antisolvent IPA is the core driving force behind the facet orientation. The purpose of incorporating IPA in the bulk phase is to extend IPA's effect instead of adding more antisolvent to flush on the surface. IPAmCl helps to stabilize the α-phase at the grain boundaries of $FAPbI_3$.

To understand the impact of the additives on the crystallization kinetics of the perovskite, we monitored the *in situ* photoluminescence (PL) during thermal annealing processes of the perovskite films, using IPA as the antisolvent. The *in situ* PL maps can be divided into two stages, corresponding to two phase transitions. The first stage occurs when IPA triggers desolvation and the conversion of solute clusters into a perovskite intermediate phase. The second stage is the thermal transformation of the intermediate into α-$FAPbI_3$. We observed that the PL intensity of IPA-PSK quenched within the first 50 seconds (the first stage), then stabilized due to further evaporation of IPA (Fig. 2f). As nucleation and crystallization proceeded, the emission peak reappeared, with the PL intensity reaching its maximum at ~350 seconds. Unlike the additive-free crystallization pathway, samples containing the IPA-based volatile additive in the bulk exhibited a slower crystallization rate, indicating that IPA(bulk)-PSK regulates the phase transition between δ-$FAPbI_3$ and α-$FAPbI_3$ (Fig. S25). However, there was still a quenching of PL intensity corresponding to the intermediate phase, indicating an increase in non-radiative recombination, likely due to the formation of FA vacancies, one of the negative effects of using IPA as an antisolvent. The rapid initial drop in PL intensity suggests insufficient repair due to IPA evaporation. When binary additives (BAs) were applied, the resulting films exhibited a slower crystallization pathway, corresponding to the later stage of Ostwald ripening (Fig. 2g).

Interestingly, when IPA and iPAmCl are used together, they cause a delayed stage of PL intensity descending range for both the first and second stages. This was due to slower antisolvent evaporation in the BA mixture, which improved solubility and led to pre-aggregation of nuclei within the precursor, altering the PL intensity evolution. These observations suggest that BAs can mitigate surface non-radiative recombination in 3D perovskite absorbers. Importantly, the BA-passivated films displayed the most optimized crystallization process compared to any single treatment. The improvements in crystallization induced by BA bulk treatment are detailed in Fig. S24–S32.

On the basis of the data presented above, we illustrate a comprehensive schematic diagram of film crystallization with IPA antisolvent (Fig. 2h). The crystallization process is decelerated by dual-additive treatment, allowing a transition from edge-sharing to corner-sharing coordination from top to bottom. This mitigates subsurface damage induced by rapid crystallization while preserving the (111) orientation. Notably, this effect occurs only when the additives are incorporated into the bulk phase. If introduced *via* the antisolvent, they interfere with the IPA-induced (111) orientation, resulting in randomly oriented films, as detailed in Fig. S33 and S34. Here, we introduce a bulk passivation method controlled by binary additives. This approach enables a progressive phase transition between δ-$FAPbI_3$ and α-$FAPbI_3$, allowing precise control over the crystallization kinetics.

Preliminary trials using the above bulk passivation strategy on 1.55 eV bandgap Br-free PSCs ($Cs_{0.05}FA_{0.85}Cs_{0.05}PbI_3$) showed a significant performance improvement, achieving a best efficiency of 24.10% using a green solvent (Fig. 3a, also see Table S1 and Fig. S35–S37). However, applying the same method to Br-containing perovskites with a 1.62 eV bandgap ($Cs_{0.05}FA_{0.9}MA_{0.05}PbI_{2.55}Br_{0.45}$) did not yield the expected results (Fig. 3b, also see Table S2 and Fig. S38). It is speculated that an unavoidable $V_{OC}$ deficit occurs in mixed-halide (Br-containing) perovskite solar cells due to light-induced phase segregation (LIPS),[14] which is mainly caused by ion migration under continuous illumination. This phenomenon is confirmed by the 3D TOF-SIMS mapping in Fig. 3c. In general, large amounts of defects tend to accelerate ion migration. We hypothesize that a destructive surface by IPA causes various defects as the ion-migration sites, so it needs to be suppressed. Aromatic ammonium cations are commonly used to passivate surfaces and inhibit phase segregation.[15,16] Based on this concept, we selected a novel passivator, trifluoromethyl-benzylamine hydroiodide ($CF_3PMAI$),[17] co-utilized with $EDAI_2$. $CF_3PMAI$ possesses a high molecular polarity (17.73 debye), which originates from the introduction of electron-withdrawing $-CF_3$ groups and the shortened alkyl chain. This high polarity suggests the large electrostatic potential, allowing the passivator to anchor more effectively on the perovskite surface, thus better suppressing phase segregation. Correspondingly, the schematic illustration and 3D TOF-SIMS evidence of suppressed LIPS after $CF_3PMAI$ surface treatment are presented in Fig. 3d and e. Perovskite films without and with $CF_3PMAI$ treatment are referred to as control and target (both with $EDAI_2$), respectively, in the following discussion. It should be noted that preliminary tests for both 1.55 and 1.62 eV perovskite compositions were carried out using the device structure: AR/ITO/3PATAT-C3 (ref. 18)/$Al_2O_3$ (ref. 19)/PSK/$EDAI_2$/$C_{60}$/BCP/Ag. Subsequently for the optimized 1.62 eV devices, we employed a modified architecture: ITO/NiOx/4PADCB[20]/PSK/$EDAI_2$/$C_{60}$/BCP/Ag. The detailed fabrication procedures can be found in the SI.

To understand the passivation mechanism of typical defects, we carried out density functional theory (DFT) calculations (Fig. 3f–h). DFT calculations revealed that bromine vacancies cause distortions in octahedra, creating shallow-level defects near the conduction band minimum (CBM). $CF_3PMAI$ treatment repairs these defects by promoting Pb–Br bonds, pushing defect states closer to the CBM.[21] For n-type defects ($Pb_I$ and $Pb_{Br}$), where Pb replaces halide, $CF_3PMAI$ corrects the octahedral distortion and eliminates deep-level trap states.[22] Similarly, for p-type defects ($I_{Pb}$ and $Br_{Pb}$), $NH^+_4$-I interactions reduce dimer interaction, inhibiting defect formation.[23] Overall, $CF_3$-PMAI's multifunctional active sites provide enhanced defect passivation through a synergistic effect, and stronger binding with the perovskite surface leads to reducing potential sites for halide segregation. The electric field generated by the interfacial dipole can also change the vacuum energy level and work function of the adjacent material (as discussed in Fig. 5). Ultraviolet photoelectron spectroscopy (UPS) measurements also revealed sub-gap defect states near the energy levels $E_{off}$ and $E_F$, which were effectively suppressed after synergistic treatment with $CF_3PMAI$.

Additionally, PL mapping visually confirmed the passivation capability of ammonium cations for mixed Br–I perovskite surfaces, including the PL intensity mapping (Fig. 3i–l) and PL lifetime mapping (Fig. 3m–p). Unsurprisingly, the control (without $CF_3PMAI$) group's PL intensity mapping showed an uneven gradient distribution, corresponding to phase segregation, which was similarly observed in the PL lifetime mapping. After treatment with $CF_3PMAI$ (denoted as target), the PL intensity and PL lifetime were both enhanced and became more uniform, indicating effective defect passivation and suppression of phase segregation. The enhancement in optoelectronic performance and stability of the perovskite films by $CF_3PMAI$, as well as the necessity of synergistic bulk and interfacial treatment for Br-containing perovskites, is demonstrated in Fig. S39S51.

The complete device architecture of PSCs is illustrated in Fig. 4a, configured as ITO/$NiO_x$/4PADCB/IPA-PSK/$EDAI_2$ without or with $CF_3PMAI$/$C_{60}$/BCP/Ag. The detailed preparation process can be found in the SI (Experimental Section). Fig. 4b shows the photocurrent density–voltage (*J–V*) curves of the champion PSCs based on different films (also see Table S3 and Fig. S52). As indicated by the inset photovoltaic parameters, the control device yields a highest PCE of 22.13% (21.86%) under reverse (forward) scan, with a $V_{OC}$ of 1.221 V (1.211 V), a short-circuit current density ($J_{SC}$) of 22.90 mA $cm^{-2}$ (22.87 mA $cm^{-2}$), and a fill factor (FF) of 79.11% (78.90%). Upon introducing $CF_3PMAI$ functional interlayers, the target device reveals enhanced $V_{OC}$ (1.243 V, 1.242 V), $J_{SC}$ (23.64 mA $cm^{-2}$, 23.51 mA $cm^{-2}$) and FF (82.83%, 81.78%), resulting in a PCE of 24.33% (23.87%), which represents one of the highest efficiencies

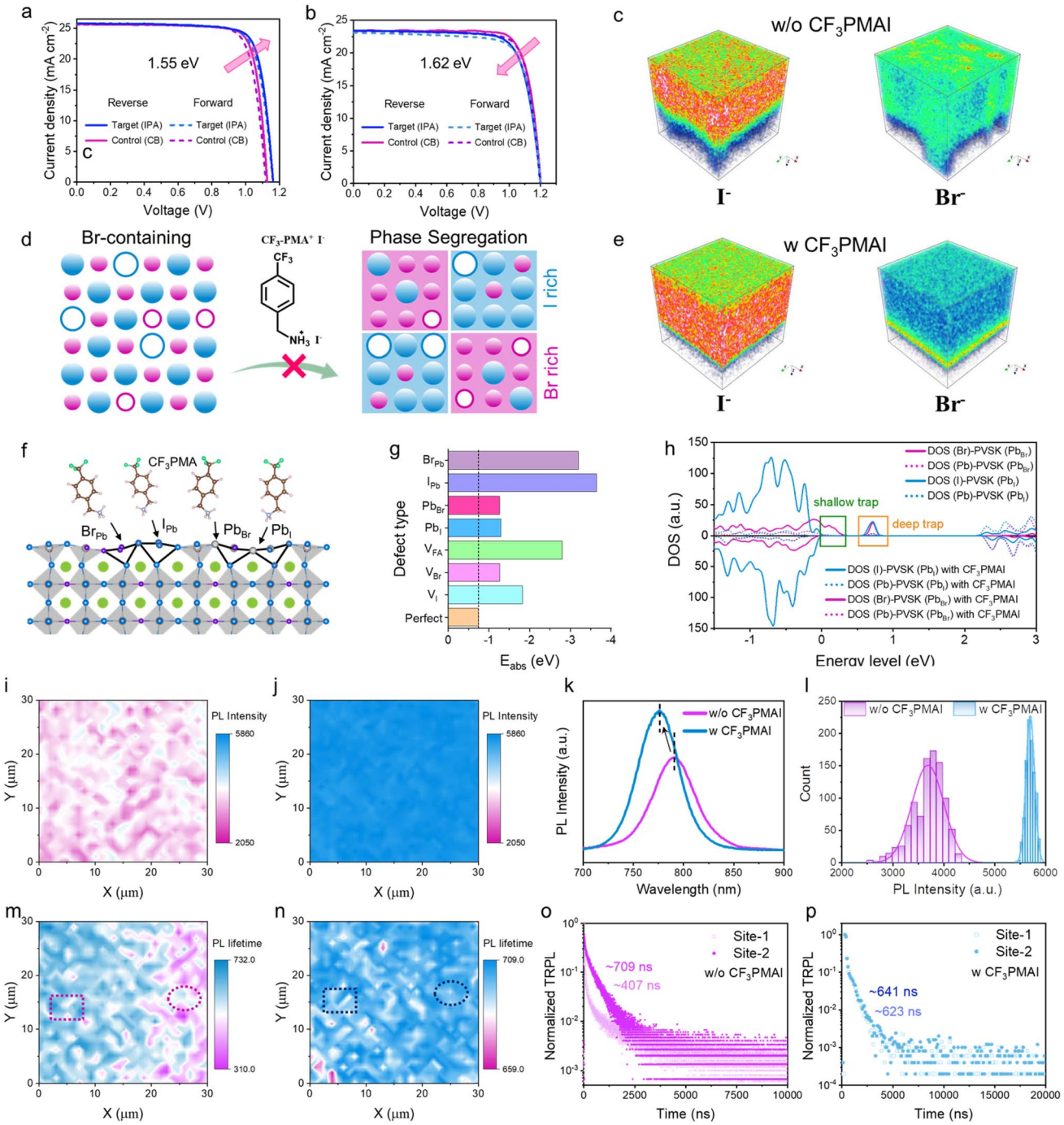


Fig. 3 Breaking the dilemma of Br-containing perovskites by IPA antisolvent. (a and b) *J*–*V* curves for both 1.55 eV and 1.62 eV PSCs. (c and e) 3D TOF-SIMS images of perovskite devices without or with $CF_3PMAI$ in negative ion mode with $I^-$ and $Br^-$. (d) Schematic illustration of the suppression mechanism of LIPS. The hollow circles denote vacancies. (f) Schematic diagram of the interaction between ammonium cations with the deep defects. (g) Absorption energy of $CF_3PMAI$ on different types of defects, with dashed lines indicating the perfect crystal reference (−0.736 eV). (h) Density of states (DOS) of control PSK and target PSK with $CF_3PMAI$ ($Pb_{Br}$ and $Pb_I$ antisite defect). PL-intensity mapping and PL-lifetime mapping of the $CF_3PMAI$-treated target perovskite film (i–l) and the untreated perovskite film (m–p).

recorded for IPA-based PSCs thus far (Fig. S53). This substantial enhancement can primarily be attributed to the improved charge carrier extraction efficiency facilitated by the stronger dipole moment associated with $CF_3PMAI$ (Fig. S54).

Fig. 4c presents that the corresponding devices without and with $CF_3PMAI$ treatment achieved steady-state power outputs of 21.97% and 24.17%, respectively, under constant AM 1.5 G illumination at the maximum power points (MPP) for 1200 s. Furthermore, the integrated $J_{SC}$ values of the control and target

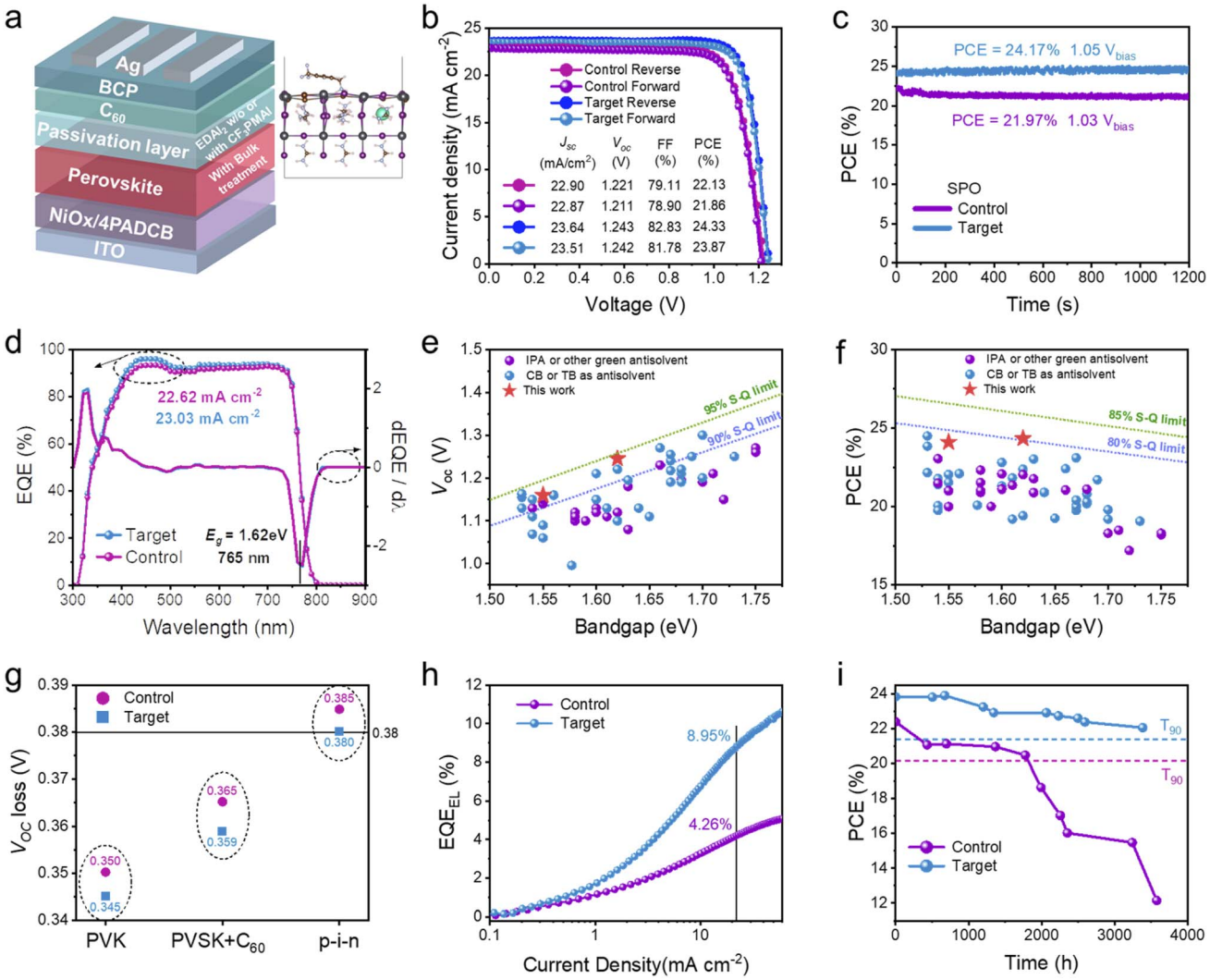


Fig. 4 Record voltage loss and efficiency. (a) Device architecture of inverted 1.62 eV PSCs. (b) *J*–*V* curves. (c) Steady-state power outputs. (d) EQE spectra, and the first derivatives of the corresponding EQE curves. (e) $V_{OC}$ and (f) PCE *versus* bandgap of high-performance PSCs reported in the literature. (g) $V_{OC}$ loss calculated from the PLQY for different perovskite samples. (h) $EQE_{EL}$ as a function of the injection current density for two types of PSCs. (i) Ambient stability of unencapsulated devices.

devices calculated from the external quantum efficiency (EQE) spectra were 22.62 and 23.03 mA $cm^{-2}$ (Fig. 4d), respectively, which aligned closely with the $J_{SC}$ values obtained from the *J*–*V* curves (Fig. 4b). The enhanced $J_{SC}$ observed in IPA-PSC is primarily attributed to improved film quality and light absorption, resulting from effective surface passivation (Fig. S55). It is worth noting that no significant shift in the bandgap is observed between the two devices, indicating that the surface treatment does not alter the perovskite phase. Instead, it facilitates sub-surface reconstruction and suppresses secondary-phase-induced interfacial reflection losses, thereby enhancing optical absorption without modifying the intrinsic band structure. The bandgaps of the perovskite films were estimated to be 1.62 eV using the first derivatives of the corresponding EQE curves, as shown in Fig. 4d. Therefore, the $V_{OC}$ loss of the best-performing PSC with IPA antisolvent was only 0.38 V.

Fig. 4e and f illustrate the PCE and $V_{OC}$ of high-performance PSCs reported in the literature (Tables S4S6), compared to the S–Q limit relative to the bandgap of the absorption layer. It is evident that most CB-PSK devices exhibit a $V_{OC}$ lower than 90% of the theoretical limit due to significant energy loss. Consequently, most device efficiencies fall below 80% of the theoretical limit. However, the champion devices, benefiting from IPA antisolvent treatment after bulk and surface engineering, achieved a $V_{OC}$ of 93% of the S–Q limit and a PCE of 80% of the S–Q limit based on a 1.62 eV perovskite. Additionally, the $V_{OC}$ loss of 0.38 V is among the lowest observed for all 1.53–1.75 eV PSCs.

The photoluminescence quantum yield (PLQY) was used to quantify the $V_{OC}$ losses ($\Delta V_{OC,loss}$) in the PSCs (Fig. 4g). It was observed that the target film led to a decrease in the $\Delta V_{OC,loss}$ of perovskite on glass ($\Delta V_{OC,loss}$ from 0.350 V to 0.345 V). Upon introducing $C_{60}$, the $\Delta V_{OC,loss}$ of the target sample only increased to 0.359 V, whereas that of the control sample

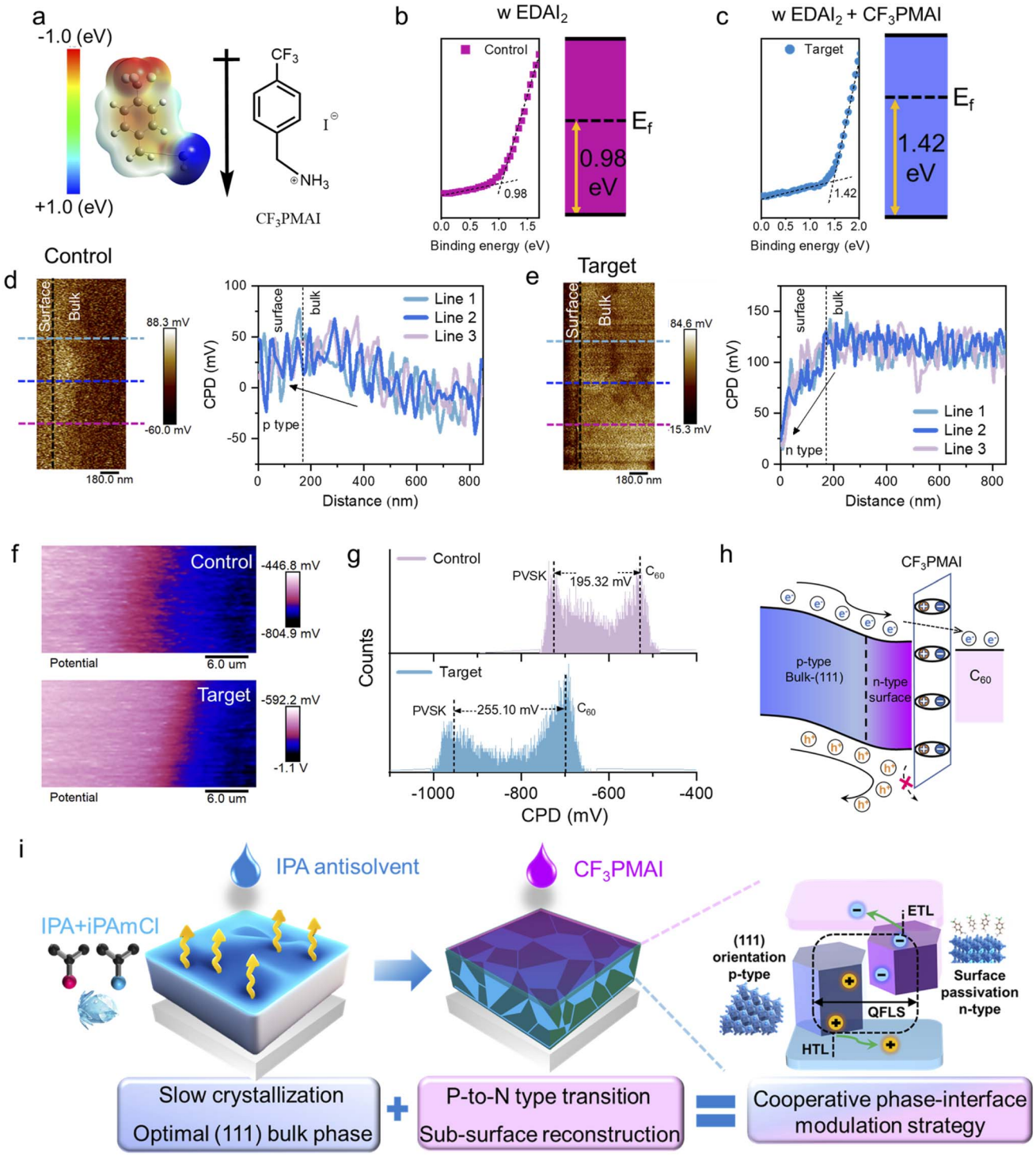


Fig. 5 Formation of a facet p–n homojunction. (a) The molecular structures of the passivators ($CF_3PMAI$) and corresponding molecular electrostatic potentials of $CF_3PMA^+$. UPS data of the upper surface of (b) control perovskite and (c) target perovskite. (d and e) The color lines of cyan, blue and purple mark the location to extract the potential profiles. (f) KPFM potential images of the control and target films with a $C_{60}$ coating on top of the perovskite layer, along with corresponding profiles of the surface potential distribution (g). Note that the purple side indicates the $C_{60}$, and the dark blue side represents the perovskite layer. (h) Band bending in interface dipole-induced perovskite. (i) Schematic illustrations of the design for the cooperative phase–interface modulation strategy.

significant increased from 0.350 V to 0.365 V. Moreover, the PSCs showed the lowest $\Delta V_{OC,loss}$ value of 0.380 V for the p-i-n target sample (SAM/PVSK/$C_{60}$ structure), which aligns well with the value derived from the $V_{OC}$. The higher PLQY observed in the target device further confirms the significant passivation effect after all-round modification.

To better quantify the nonradiative recombination-induced $V_{OC}$ loss/deficit ($\Delta V_{OC,\ non\text{-}rad}$), it was calculated using the following formula:

$$\Delta V_{OC,non\text{-}rad} = -\frac{k_B T}{q} \ln(EQE_{EL})$$

Electroluminescence quantum efficiency ($EQE_{EL}$) measurements were performed and the results are shown in Fig. 4h. The higher $EQE_{EL}$ value of over 8.95% for the target PSC at a current density of ~23.00 mA $cm^{-2}$ (simulated open circuit) compared to 4.26% for the control device demonstrates effectively suppressed non-radiative recombination losses in IPA custom-tailored PSCs. As a result, the target device exhibits a lower $\Delta V_{OC,\ non\text{-}rad}$ of 62.5 mV than 81.7 mV of the control one, consistent with the quasi-Fermi level splitting (QFLS) results calculated from the PLQY, and therefore an increased $V_{OC}$ output. Details of the $EQE_{EL}$ results and additional characterization studies with synergistic $CF_3$PMAI surface treatment are provided in Fig. S56-58.

We then investigated the PCEs of the unencapsulated PSCs for evaluating their long-term stability (Fig. 4i). As expected, the target device exhibits significantly enhanced long-term stability, retaining approximately 90% of its initial efficiency after over 3000 hours of aging under ambient air conditions (25 °C, 30–40% RH). In contrast, the control device drops below the $T_{90}$ threshold at around 2000 hours and subsequently undergoes rapid performance degradation.

In the following sections, the origin of the superior $V_{OC}$ of target PSCs will be studied and revealed in detail. Compared to bulk passivation, surface treatment resulted in a more pronounced increase in $V_{OC}$, which is typically associated with the establishment of a stronger built-in electric field. In contrast, the electric field generated by the interfacial dipole can also alter the vacuum energy level and work function of the surface's electrical properties. The molecular structure of $CF_3$-PMAI has a high dipole moment, pointing from the ammonium group to the electronegative $-CF_3$ at the other end (Fig. 5a). This high dipole moment indicates a significant difference in electrostatic potential between the two ends of the molecule. To probe the improved capability of target perovskites, we conducted the UV-vis absorption test and ultraviolet photoelectron spectroscopy (UPS) on perovskite films. The Fermi level ($E_f$) of the target film shifted from closer to the valence band to closer to the conduction band, which signifies a transition of the perovskite from p-type to n-type, according to the UPS result, as shown in Fig. 5b and c. This result suggests that the concentration of background hole carriers in the target sample was reduced, indicating successful surface reconstruction and removal of secondary crystal facets, as well as suppression of the p-type $PbI_2$ phase.

To gain deeper insights into the influence of $CF_3$PMAI on the energy level of perovskite, cross-sectional Kelvin probe force microscopy (KPFM) is further conducted in the perovskite film to investigate the cross-sectional potential distribution (Fig. 5d, e and S59-S62). Interestingly, the target perovskite was more n-type than that of control perovskite on the surface, as shown in Fig. 5e. In the target perovskite, the potential obviously starts to decrease, especially at top surface regions (≈−120 mV), indicating its relative n-type surface in comparison with the perovskite bulk. In contrast, the potential slightly increases and reaches ≈+50 mV at the top surface region in the control perovskite, indicating its relative p-type surface in comparison with the perovskite bulk. Importantly, these findings are consistent with the previous UPS results. We propose that the n-type sub-surface region in the top will spontaneously form a planar p–n homojunction[24] with the underneath p-type character (111)-$FAPbI_3$ region in the perovskite active layer of PSCs.[25] According to the energy level alignment schematics shown in Fig. S58, the (111)-oriented perovskite exhibited more p-type characteristics compared to the (100)-oriented perovskite, consistent with our previous report. Simultaneously, the incorporated $CF_3$PMAI likely generates an augmented built-in electric field between the n-type sub-surface and the p-type (111)-perovskite, facilitating the efficient separation of photogenerated carriers and increasing the $V_{OC}$ of the target PSCs. These results collectively demonstrate the design rationale of our cooperative phase–interface modulation strategy, which underpins the realization of the high $V_{OC}$ and PCE, as illustrated in Fig. 5i.

We further compared the variations in interfacial potential between the perovskite and $C_{60}$ (ref. 26) in Fig. 5f. The corresponding surface CPD (Fig. 5g) across the perovskite/$C_{60}$ interface exhibited that the target film (255.10 mV) had a bigger CPD value than that of the control film (195.32 mV), respectively. The target film undergoes a shift towards negative potential values and exhibits a larger potential difference with $C_{60}$, providing a sufficient explanation for the enhanced extraction of electron carriers at the interface of the target film. The resulting energy level alignment will boost charge transport and thus reduce charge recombination at the perovskite/$C_{60}$ interface of PSCs (Fig. 5h).

## Conclusion

In summary, this work addresses the critical challenge of employing green IPA antisolvent, specifically in bromide-containing perovskite solar cells, which are prone to phase segregation and suffer from consequential $V_{OC}$ losses. We systematically explored the impact of surface and bulk regulation on (111)-oriented 1.62 eV-bandgap perovskite films.

For the first time, we identified a topological correlation between the (002)-oriented δ-$FAPbI_3$ phase and the (111)-oriented α-phase. By coupling this finding with the same umbrella-like bulk binary additives (IPA + iPAmCl), we guided the formation of a (111)-oriented transformation pathway and effectively modulated the crystallization kinetics, resulting in highly (111)-textured and defect-suppressed perovskite films. Subsequently, the rationally designed passivation molecule $CF_3$PMAI regulated dipole moment and interfacial compatibility. Complementary surface passivation with $CF_3$PMAI effectively suppressed halide phase segregation and induced a p-to-n surface transition. We propose that the resulting n-type sub-surface spontaneously forms a p–n facet homojunction

with the underlying p-type (111)-$FAPbI_3$ region, thereby enhancing the quasi-Fermi level splitting and reducing the open-circuit voltage loss.

As a result of this integrated strategy, the Br-containing 1.62 eV PSCs achieved an ultrahigh $V_{OC}$ of 1.24 V and a record PCE of 24.33%, along with robust storage stability (20% degradation ($T_{80}$) after over 3000 h under ambient air conditions (25 °C, 30–40% RH)). Importantly, this study demonstrates the first successful use of green IPA antisolvent in Br-containing perovskites *via* an environmentally benign process. The mechanistic understanding of facet and defect engineering presented here provides a general design principle for pushing $V_{OC}$ toward its fundamental limits in perovskites.

## Conflicts of interest

A. W. is a co-founder and Chief Advisor (Science & Technology) of EneCoat Technologies Co., Ltd.

## Data availability

All data are available in the main text or the supplementary information (SI). Supplementary information is available. See DOI: https://doi.org/10.1039/d5el00189g.

## Acknowledgements

This work was supported by the Strategic Priority Research Program of the Chinese Academy of Sciences (Grant No. XDB1140101). This work was conducted by the Fundamental Research Center of Artificial Photosynthesis (FReCAP), with financial support from DICP (Grant: DICP I202469) and the National Natural Science Foundation of China (22088102). The authors extend their gratitude to the Theoretical and Computational Chemistry Team (from Scientific Compass https://www.shiyanjia.com) for providing invaluable assistance. This work was supported by the International Collaborative Research Program of ICR (Kyoto University), Grant-in-Aid for Scientific Research (A) (JP24H00481), and Grant-in-Aid for Scientific Research (B) (JP24K01571).

## References

1 A. D. Taylor, Q. Sun, K. P. Goetz, Q. An, T. Schramm, Y. Hofstetter, M. Litterst, F. Paulus and Y. Vaynzof, *Nat. Commun.*, 2021, **12**, 1878.
2 L. Chao, T. Niu, W. Gao, C. Ran, L. Song, Y. Chen and W. Huang, *Adv. Mater.*, 2021, **33**, 2005410.
3 X. Sun, D. Li, L. Zhao, Y. Zhang, Q. Hu, T. P. Russell, F. Liu, J. Wei and H. Li, *Adv. Mater.*, 2023, **35**, 2301115.
4 S. Qu, H. Huang, J. Wang, P. Cui, Y. Li, M. Wang, L. Li, F. Yang, C. Sun, Q. Zhang, P. Zhu, Y. Wang and M. Li, *Angew. Chem., Int. Ed.*, 2025, **64**, e202415949.
5 Y. Wang, J. Wu, P. Zhang, D. Liu, T. Zhang, L. Ji, X. Gu, Z. David Chen and S. Li, *Nano Energy*, 2017, **39**, 616–625.
6 B. Zhou, P. Zhao, J. Guo, S. Hu, X. Guo, J. Liu and C. Li, *Energy Environ. Sci.*, 2025, **18**, 9865–9876.
7 S. Tan, T. Huang, I. Yavuz, R. Wang, M. H. Weber, Y. Zhao, M. Abdelsamie, M. E. Liao, H.-C. Wang, K. Huynh, K.-H. Wei, J. Xue, F. Babbe, M. S. Goorsky, J.-W. Lee, C. M. Sutter-Fella and Y. Yang, *J. Am. Chem. Soc.*, 2021, **143**, 6781–6786.
8 Y. Li, Z. Shi, J. Li, B. Li, R. Jiang, C. Jin, S. Kong, Y. Peng, B. Xue, F. Huang, Y.-B. Cheng and T. Bu, *Adv. Funct. Mater.*, 2025, **35**, 2506206.
9 Y. Feng, Q. Chen, X. Yan, X. Fu, D. Wang, Z. Ding, S. Li, C. Geng, L. Gao, J. Zhang, F. Yang, S. M. H. Qaid, S. Gao, Y. Jiang and M. Yuan, *Angew. Chem., Int. Ed.*, 2024, **63**, e202412685.
10 J. Jiang, C. Tian, Z. Zhang, X. (Xiao) Liu, X. Wang, Y. Zheng, Z. Zhang, L. Wang, X. Wu, J. Liang and C.-C. Chen, *Mater. Adv.*, 2022, **3**, 5786–5795.
11 G. Yang, Z. Ren, K. Liu, M. Qin, W. Deng, H. Zhang, H. Wang, J. Liang, F. Ye, Q. Liang, H. Yin, Y. Chen, Y. Zhuang, S. Li, B. Gao, J. Wang, T. Shi, X. Wang, X. Lu, H. Wu, J. Hou, D. Lei, S. K. So, Y. Yang, G. Fang and G. Li, *Nat. Photonics*, 2021, **15**, 681–689.
12 D. Prat, J. Hayler and A. Wells, *Green Chem.*, 2014, **16**, 4546–4551.
13 B. Park, H. W. Kwon, Y. Lee, D. Y. Lee, M. G. Kim, G. Kim, K. Kim, Y. K. Kim, J. Im, T. J. Shin and S. I. Seok, *Nat. Energy*, 2021, **6**, 419–428.
14 Y. Guo, X. Yin, J. Liu and W. Que, *Matter*, 2022, **5**, 2015–2030.
15 T. Li, J. Xu, R. Lin, S. Teale, H. Li, Z. Liu, C. Duan, Q. Zhao, K. Xiao, P. Wu, B. Chen, S. Jiang, S. Xiong, H. Luo, S. Wan, L. Li, Q. Bao, Y. Tian, X. Gao, J. Xie, E. H. Sargent and H. Tan, *Nat. Energy*, 2023, **8**, 610–620.
16 R. Chen, J. Wang, Z. Liu, F. Ren, S. Liu, J. Zhou, H. Wang, X. Meng, Z. Zhang, X. Guan, W. Liang, P. A. Troshin, Y. Qi, L. Han and W. Chen, *Nat. Energy*, 2023, **8**, 839–849.
17 Y. Shi, Y. Zhang, H. Guo, Y. Zhang, M. Li, C. Xiao, W. Huang, Y. Zhai, J. Xia, E. Aydin and F. Zhang, *Joule*, 2025, 102009.
18 M. A. Truong, T. Funasaki, L. Ueberricke, W. Nojo, R. Murdey, T. Yamada, S. Hu, A. Akatsuka, N. Sekiguchi, S. Hira, L. Xie, T. Nakamura, N. Shioya, D. Kan, Y. Tsuji, S. Iikubo, H. Yoshida, Y. Shimakawa, T. Hasegawa, Y. Kanemitsu, T. Suzuki and A. Wakamiya, *J. Am. Chem. Soc.*, 2023, **145**, 7528–7539.
19 M. A. Truong, T. Funasaki, Y. Adachi, S. Hira, T. Tan, A. Akatsuka, T. Yamada, Y. Iwasaki, Y. Matsushige, R. Kaneko, C. Asahara, T. Nakamura, R. Murdey, H. Yoshida, Y. Kanemitsu and A. Wakamiya, *J. Am. Chem. Soc.*, 2025, **147**(3), 2797–2808.
20 Z. Wang, Z. Han, X. Chu, H. Zhou, S. Yu, Q. Zhang, Z. Xiong, Z. Qu, H. Tian, W. Wang, F. Wan, Y. Yuan, Y. Lin, Y. Yang, X. Zhang, Q. Jiang and J. You, *Adv. Mater.*, 2024, **36**, 2407681, DOI: 10.1002/adma.202407681.
21 J. Chen, Y. Yang, H. Dong, J. Li, X. Zhu, J. Xu, F. Pan, F. Yuan, J. Dai, B. Jiao, X. Hou, A. K.-Y. Jen and Z. Wu, *Sci. Adv.*, 2022, **8**, eabk2722.
22 J. M. Ball and A. Petrozza, *Nat. Energy*, 2016, **1**, 1–13.
23 X. Qiao, R. Zhu, D. Yan, Z. Su, Z. Zhang, H. Wu, Y. Tan, M. Liang, W. Zuo, J. Zhang, G. Li, X. Gao, M. Saliba and M. Li, *Adv. Funct. Mater.*, 2024, **34**, 2409852.

24 S. Xiong, Z. Hou, S. Zou, X. Lu, J. Yang, T. Hao, Z. Zhou, J. Xu, Y. Zeng, W. Xiao, W. Dong, D. Li, X. Wang, Z. Hu, L. Sun, Y. Wu, X. Liu, L. Ding, Z. Sun, M. Fahlman and Q. Bao, *Joule*, 2021, **5**, 467–480.
25 F. Gao, H. Li, B. Jiao, L. Tan, C. Deng, X. Wang, C. Luo, C. Zhan, E. Debroye, Y. Peng, Y. Yang, C. Yi and Q. Zhao, *Joule*, 2025, **9**, 101787.
26 Z. Liu, H. Li, Z. Chu, R. Xia, J. Wen, Y. Mo, H. Zhu, H. Luo, X. Zheng, Z. Huang, X. Luo, B. Wang, X. Zhang, G. Yang, Z. Feng, Y. Chen, W. Kong, J. Gao and H. Tan, *Adv. Mater.*, 2024, **36**, 2308370.